Magnetic Resonances of ^{51}V, ^{209}Bi, Mn^{2+}, and Fe^{3+} in $BiVO_4$ Single Crystals *

Sung Ho Choh

Department of Physics, Korea University, Seoul 136-701, Republic of Korea

Z. Naturforsch. **51a**, 591–602 (1996); received February 3, 1996

Nuclear magnetic resonance (NMR) of ^{51}V and ^{209}Bi, and electron paramagnetic resonance (EPR) of Mn^{2+} and Fe^{3+} impurities in ferroelastic $BiVO_4$ single crystals are reviewed. The nuclear quadrupole parameters and principal axes of the two host nuclei, ^{51}V and ^{209}Bi, and the second-order zero field splitting tensor of the isoelectronic $3d^5$ ions, Mn^{2+} and Fe^{3+}, in $BiVO_4$ are determined for the first time. Temperature dependence studies on ^{51}V NMR and Mn^{2+} EPR confirmed that this crystal undergoes a second order phase transition. The substitutional sites of Mn^{2+} and Fe^{3+} in $BiVO_4$ are Bi^{3+} and V^{5+}, respectively.

Key words: NMR, EPR, Quadrupole parameters, Zero field splittings, Substitutional sites.

Introduction

Bismuth vanadate ($BiVO_4$) was first synthesized by Roth and Waring [1] in 1963, and was found to be ferroelastic by Bierlein and Sleight [2] in 1975. Since then, there have been a great deal of experimental investigations such as x-ray diffraction [3], neutron diffraction [4], Raman scattering [5, 6], nuclear magnetic resonance (NMR) [7] and electron paramagnetic resonance (EPR) [8, 9] to study the structural changes, phase transitions and optical properties. Ferroelastics have received considerable attention in recent years, and the $BiVO_4$ crystal may prove to be a promising material for acousto-optics [10].

In this paper, the quadrupole coupling constant, the asymmetry parameter and the directions of the principal axes of the electric field gradient (efg) tensor are discussed for the ^{51}V [11] and ^{209}Bi [12] nuclei in $BiVO_4$ single crystals. ^{51}V and ^{209}Bi are both 100% naturally abundant with nuclear spin of 7/2 and 9/2, respectively. EPR of Mn^{2+} [13, 14] and Fe^{3+} [15] contained in $BiVO_4$ crystals as impurities has been investigated using X- and Q-band spectrometers. The relationship between the principal axes of the zero field splitting (zfs) tensor and crystallographic axes is examined by means of the rotation patterns of the EPR spectra and is discussed in terms of the defect structure. The temperature dependence of the quadrupole parameters of ^{51}V [16] and zfs parameters of Mn^{2+} [17] has also been studied. The phase transition temperature and its nature of transition of $BiVO_4$ crystal may also be determined by NMR and EPR techniques. The substitutional sites of Mn^{2+} [17] and Fe^{3+} [18] in $BiVO_4$ were proposed from experiments and theoretical calculations.

* Presented at the XIIIth International Symposium on Nuclear Quadrupole Interactions, Providence, Rhode Island, USA, July 23–28, 1995.

Reprint requests to Prof. Sung Ho Choh.

1. Crystal Structure

It is known that this material undergoes a reversible second-order phase transition at about 523 K between the monoclinic fergusonite structure (space group $I2/a\,(C_{2h}^6)$) and the tetragonal scheelite (space group $I4_1/a\,(C_{4h}^6)$) structure [19]. The paraelastic tetragonal structure of $BiVO_4$ is shown in Fig. 1, where the structural parameters are $a = c = 5.1509$ Å, and $b = 11.730$ Å at 573 K. At room temperature the lattice parameters are $a = 5.1966$, $b = 11.704$, $c = 5.0921$ Å, and $\beta = 90.384°$. The monoclinic phase has distortions from the scheelite structure due to small displacements of Bi^{3+} and V^{5+} cations along the b-axis [4]. The displacements of Bi^{3+} play a major role in the transition [20]. In the ferroelastic phase, the vanadium atom is located with different bond lengths ($V\text{-}O_I$ and $V\text{-}O_{II}$) in a distorted oxygen tetrahedron, and the bismuth atom is coordinated by eight distorted VO_4 tetrahedra. The crystallographic data show that the monoclinic axis is parallel to the crystallographic b-axis [21], and the crystal may be treated as

0932-0784 / 96 / 0500-0591 $ 06.00 © – Verlag der Zeitschrift für Naturforschung, D-72072 Tübingen

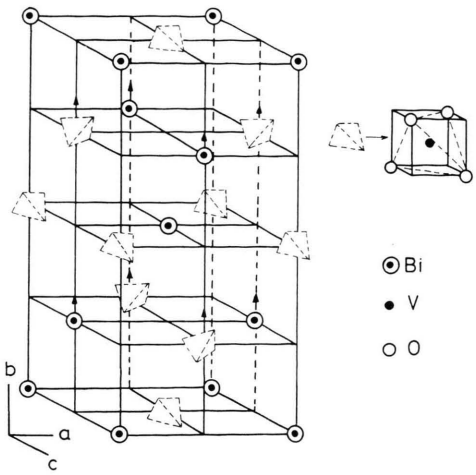

Fig. 1. The crystal structure of $BiVO_4$ in the paraelastic phase above T_c.

orthorhombic as an approximation due to the fact that $\beta = 90.384°$ is so close to 90.0°.

2. Experimental Results and Analysis

$BiVO_4$ single crystals were grown by the Czochralski method from a mixture of Bi_2O_3(3N) and V_2O_5(3N) powder [6]. The orientation of the specimen was determined by the x-ray Laue method [11].

2.1 NMR of ^{51}V

NMR of ^{51}V ($I = 7/2$) has been investigated in the ferro- and paraelastic phase of $BiVO_4$. The seven line structure of ^{51}V is due to the quadrupole interaction of the vanadium nucleus which has the nuclear spin of 7/2 as shown in Figure 2. A WL-112 Varian NMR spectrometer was employed. The rotation patterns measured in the *ab*-, *bc**-, and *c** *a*-plane as shown in Fig. 3 a turned out to be in the principal planes of the efg tensor. The *c**-axis was chosen to be perpendicular to the *ab*-plane, but it is nearly parallel to the *c*-axis, since β is slightly different from 90.0°. The maximum separation due to the quadrupole interaction was observed when the magnetic field was applied along the *b*-axis of the crystal, and this direction is analyzed to be the *Z*-axis of the efg tensor. The resonance fields in the ferroelastic phase show angular dependence, whereas no angular dependence was observed in the *ac**-plane above T_c, as shown in Figure 3 b.

2.2 NMR of ^{209}Bi

The ^{209}Bi nucleus has the nuclear spin $I = 9/2$, which may lead to nine allowed NMR transitions. However, as a result of large quadrupole interaction and wide linewidths, the detected signals were very weak, and the signal-to-noise ratio was only 3 to 1 as shown in Figure 4. At best only three lines due to a large quadrupole interaction were measured at a fixed frequency of 6 MHz in the crystallographic planes. The rotation patterns measured in crystallographic planes turned out to be different from the principal planes of the efg tensor, as shown in Figure 5. However, the maximum separation of the pattern was extrapolated to the *b*-axis of the crystal.

2.3 NMR Hamiltonian

The Hamiltonian to analyze these NMR results is as usual

$$H = H_Z + H_Q\,, \tag{1}$$

where H_Z is the nuclear Zeeman term and H_Q describes the nuclear quadrupole interaction of the resonant nucleus (^{51}V and ^{209}Bi, respectively). The Zeeman interaction is given by

$$H_Z = -\,g_n \beta_n \boldsymbol{B} \cdot \boldsymbol{I}\,, \tag{2}$$

where g_n is the nuclear g-factor, β_n the nuclear magneton $\left(= \dfrac{e\hbar}{2m_p} = 5.05082 \times 10^{-27}\ \mathrm{J/T}\right)$, B the mag-

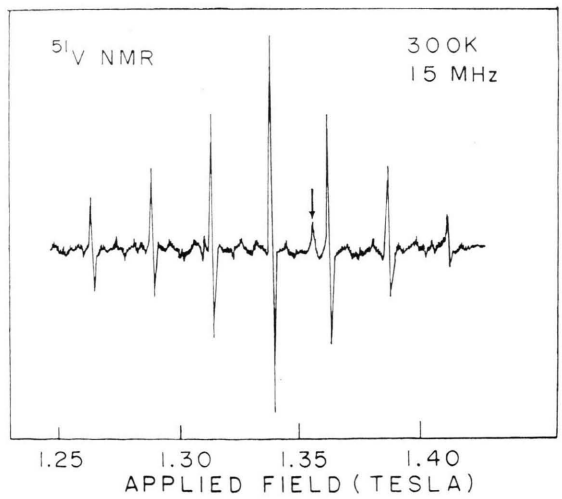

Fig. 2. Typical spectra of ^{51}V NMR in $BiVO_4$ showing the seven line structure. The signal marked with an arrow is the ^{27}Al line from the NMR probe.

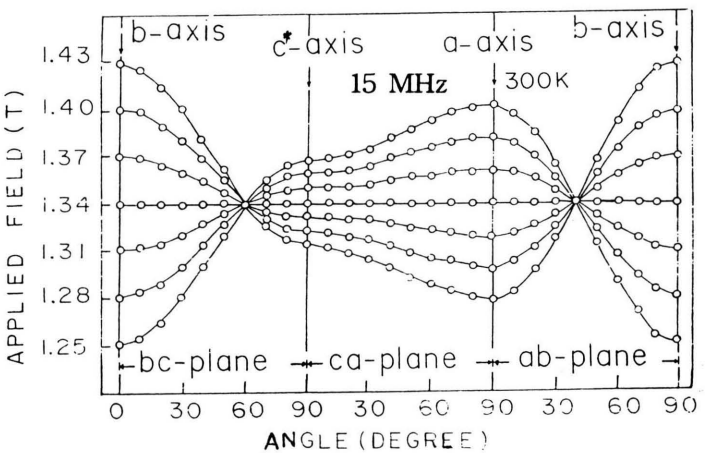

a)

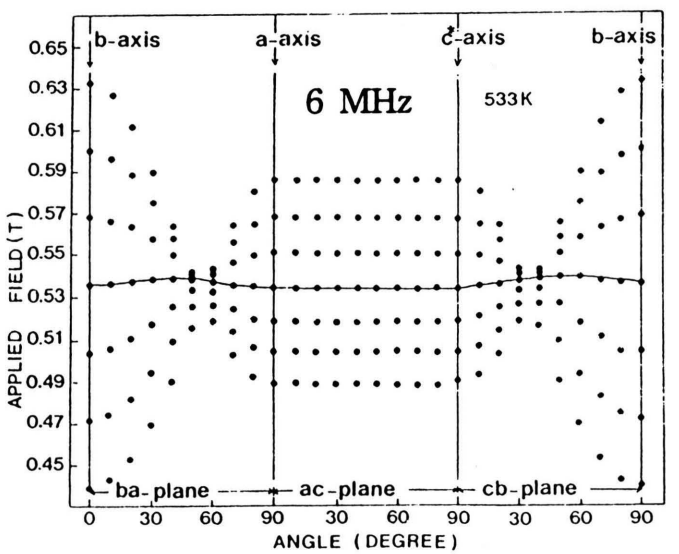

b)

Fig. 3. Rotation patterns of ^{51}V NMR, a) in the ferroelastic and b) in the paraelastic phase. Lines in a) are calculated with the best fit parameters.

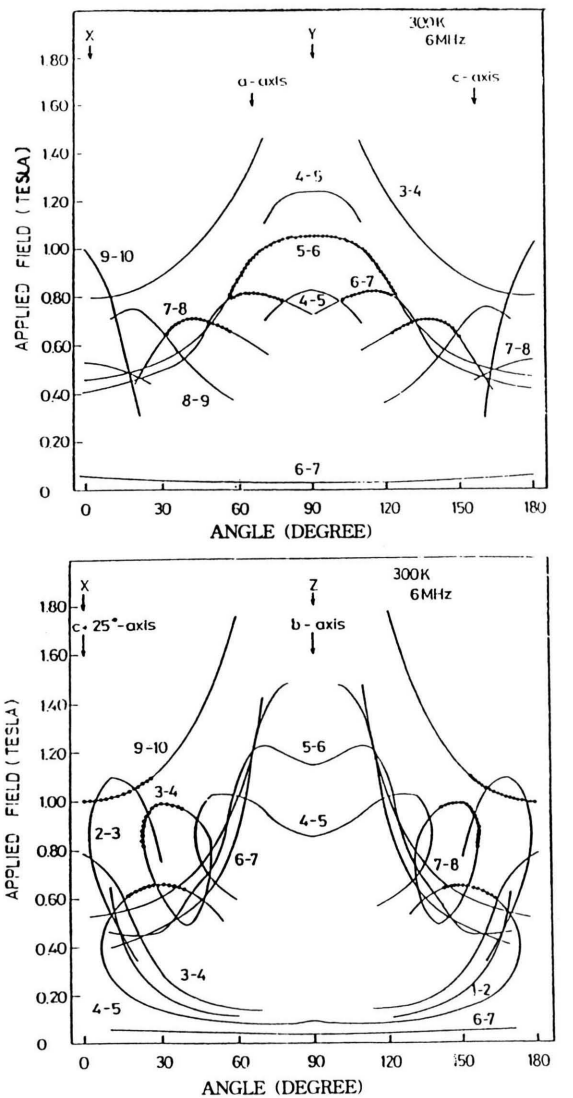

Fig. 5. Rotation patterns of ^{209}Bi NMR, a) in the *ac*-plane and b) a principal plane of the efg tensor. Curves are calculated based on the best fit parameters. Dots are experimental data.

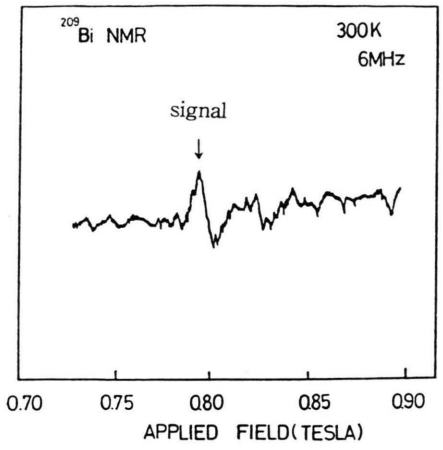

Fig. 4. A typical NMR signal of ^{209}Bi in $BiVO_4$.

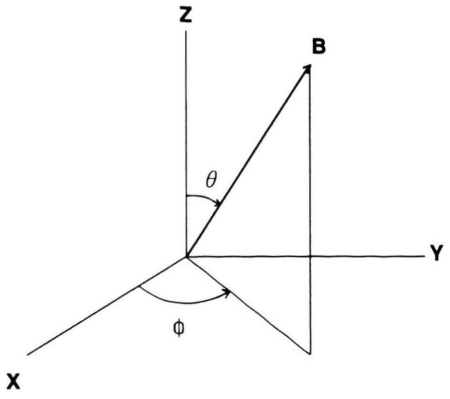

Fig. 6. The direction of the static magnetic field is referred to the principal axes of the efg tensor with the polar angle θ and azimuthal angle ϕ.

netic field and I the nuclear spin. The quadrupole Hamiltonian in the principal axis system of the electric field gradient tensor is given by

$$H_Q = \frac{e^2 qQ}{4I(2I-1)}\left[3I_Z^2 - I(I+1) + \frac{1}{2}\eta(I_+^2 + I_-^2)\right], \quad (3)$$

where $e^2 qQ/h$ is the quadrupole coupling constant and η the asymmetry parameter. The conventional X, Y, and Z axes are such that $|V_{XX}| \leq |V_{YY}| \leq |V_{ZZ}| = \text{eq}$; then $0 \leq \eta \leq 1$.

Calculation of the energy eigenvalues of (1) requires the simultaneous diagonalization, usually performed numerically by a computer program. However, for the case of $|H_Z| \gg |H_Q|$, the perturbation theory gives us better insight into the problem. When we use the principal axes of the efg tensor as the reference frame, as shown in Fig. 6, the energy eigenvalues of (1) for the nuclear state $|I, m>$ may be given by

$$E_m = E_m^{(0)} + E_m^{(1)} + E_m^{(2)} + \cdots,$$

where $E_m^{(0)} = -g_n \beta_n B m$,

$$E_m^{(1)} = \frac{e^2 qQ}{4I(2I-1)}\{3m^2 - I(I+1)\} \cdot \left[\frac{1}{2}(3\cos^2\theta - 1) + \frac{1}{2}\eta \sin^2\theta \cos 2\phi\right]. \quad (4)$$

NMR transitions are induced by the oscillating (frequency ν) magnetic field which is applied perpendicular to the strong static magnetic field. Thus, transitions obey the selection rule $\Delta m = \pm 1$, and the resonance condition of $h\nu = E_{m-1} - E_m$ gives us the resonance magnetic field as

$$B_m^{\text{res}} = \frac{h\nu}{g_n \beta_n} - \frac{1}{g_n \beta_n}\frac{3e^2 qQ}{2I(2I-1)}\left(m - \frac{1}{2}\right) \cdot \left[\frac{1}{2}(3\cos^2\theta - 1) + \frac{1}{2}\eta \sin^2\theta \cos 2\phi\right] + \cdots. \quad (5)$$

The quadrupole parameters of ^{51}V in $BiVO_4$ are calculated with (5), using the rotation patterns shown in Fig. 3a measured in three mutually perpendicular planes. For the analysis of Fig. 3b, the second order perturbation term was necessary due to the reduced Zeeman term from 15 MHz (Fig. 3a) down to 6 MHz (Fig. 3b) of the NMR frequency. However, the rotation pattern of ^{209}Bi is totally different from that of ^{51}V, thus (5) is no longer applicable to ^{209}Bi. Consequently, a computer program of numerical diagonalization of the eigenvalues of (1) was employed to obtain the quadrupole parameters of ^{209}Bi in $BiVO_4$.

The quadrupole parameters of ^{51}V and ^{209}Bi in $BiVO_4$ are summarized in Table 1. However, the quadrupole parameters of ^{209}Bi turned out to be quite different from those in a previous report [7], obtained with a ceramic sample at liquid-nitrogen temperature. The quadrupole moment Q of ^{51}V and ^{209}Bi is -4×10^{-30} and -4×10^{-29} m^2, respectively [24]. Thus q at Bi is about 1.6 times stronger than that at V in $BiVO_4$. While the principal axes of the efg tensor for ^{51}V are along the crystallographic axes, those for ^{209}Bi are found to be along the crystallographic $c^* + 25°$, $a + 25°$ and b-axis, respectively. The relation between the principal axes of the efg tensor and the

Table 1. Quadrupole parameters of ^{51}V and ^{209}Bi in $BiVO_4$.

Nucleus	e^2qQ/h (MHz)	η	Principal axes of efg	Temperature (K)	Sample	Ref.
^{51}V	5.062	0.459	$X=c^*$, $Y=a$, $Z=b$	77	crystal	[11]
	4.856[a]	0.380	$X=c^*$, $Y=a$, $Z=b$	300	crystal	[11]
	5.031	0	$Z=b$	533	crystal	[22]
^{209}Bi			$X=c^*+25°$			
	79.2±0.1	0.70±0.01	$Y=a+25°$	300	crystal	[12]
			$Z=b$			
	149 ±5	0.9 ±0.1		77	ceramic	[7]

[a] This value is confirmed independently [23].

crystallographic axes for ^{51}V and ^{209}Bi is shown in Figure 7.

2.4 EPR of Mn^{2+}

The manganese ion was not doped by us into the crystal but was in the starting material as an impurity. A typical spectrum of Mn^{2+} in $BiVO_4$ obtained with an X-band spectrometer is shown in Figure 8. The five groups of lines are the fine structure of Mn^{2+} ($S=5/2$), and the six lines within each group are the hyperfine structure of ^{55}Mn ($I=5/2$, 100% abundance). For the EPR measurements a Bruker EPR spectrometer (ESP 300 series) was used. The rotation patterns of the fine structure on the crystallographic *ab*-, *bc**-, and *c***a*-planes were obtained at 1° or 2° intervals and displayed in Figures 9 and 10. From the experimental data for the three crystallographic planes, the accuracy of the sample alignment is estimated to be within ± 1.0°.

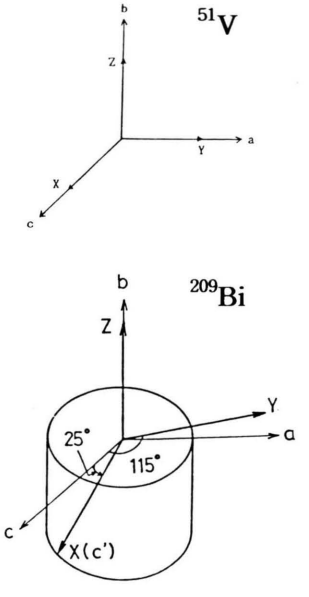

Fig. 7. The principal axes of the efg tensor for ^{51}V and ^{209}Bi in $BiVO_4$ at room temperature.

The data points of Mn^{2+} resonance in Fig. 9 show a symmetric angular dependence. Thus, one principal axis of the zero-field splitting tensor automatically turns out to be along the *b*-axis for which the rotation patterns are symmetric on the *ab*- and *bc**-planes. Consequently, the remaining two principal axes are on the *c** *a*-plane, perpendicular to the *b*-axis. Accordingly, from the angular dependence of the resonance fields on the *c** *a*-plane (Fig. 10), the two other principal axes of the zero-field splitting tensor are determined to be $c^*+45°$ and $a+45°$, respectively. The maximum separation of the resonance fields due to the **D**-tensor was observed when the magnetic field was applied along the $a+45°$ direction in the *c** *a*-plane of the crystal, and this direction was designated as the *Z*-axis of the **D**-tensor.

2.5 EPR of Fe^{3+}

The rotation patterns of the resonance fields of Fe^{3+} in $BiVO_4$ were obtained at room temperature on the crystallographic *ab*-, *bc**-, and *c** *a*-plane with a Q-band spectrometer instead of X-band, and displayed in Figures 11 and 12. The data points in the *ab*- and *bc**-plane show a symmetric angular dependence. One principal axis of the zfs tensor automatically turns out to be along the *b*-axis, for which the rotation patterns are symmetric on the *ab*- and *bc**-plane. Consequently, the remaining two principal axes are on the *c** *a*-plane, perpendicular to the *b*-axis. Accordingly, from the angular dependence of the resonance fields

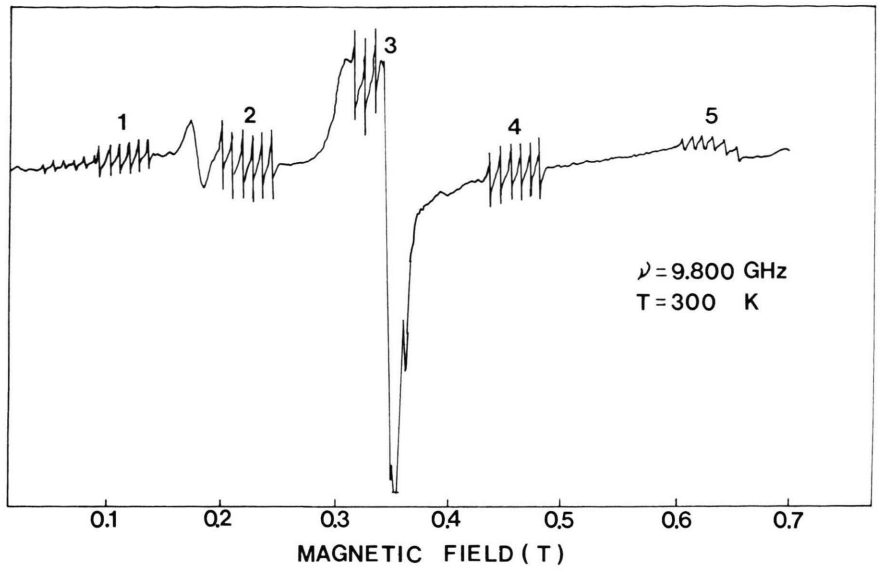

Fig. 8. Typical EPR spectra of Mn^{2+} in $BiVO_4$. There are other unidentified signals. Very weak signals below 0.1 T are the forbidden transition of Mn^{2+} with $\Delta M = \pm 2$ (see Figure 10).

on the c^*a-plane the two other principal axes of the zfs tensor are determined to be about $c^* + 30°$ and $a + 30°$, respectively. The maximum separation of the resonance fields due to the **D**-tensor was extrapolated to the b-axis when the magnetic field was applied along the b direction in the ab- and bc^*-planes of the crystal, and this direction was designated as the Z-axis of **D**-tensor.

2.6 *Spin Hamiltonian*

The Mn^{2+} and Fe^{3+} are isoelectronic with the electron configuration $3d^5$ and are S-state ions with $S = 5/2$ and basic level of $^6S_{5/2}$. The fine structure of both ions results from the crystal field, spin-orbit, and spin-spin interactions, and the hyperfine structure of Mn^{2+} originates from the interaction between the nuclear spin of ^{55}Mn and its electronic spin. Accordingly, the experimental results for the resonance fields can be analyzed with the usual spin Hamiltonian

$$H = H_Z + H_{zfs} + H_h + H_{nZ} + H_Q , \tag{6}$$

where the terms on the right-hand side are the electronic Zeeman, the zero field splitting, the hyperfine, the nuclear Zeeman, and the quadrupole interaction, respectively. The terms in (6) may be expressed as

$$\begin{aligned} H_Z &= \beta \boldsymbol{B} \cdot \overleftrightarrow{\mathbf{g}} \cdot \boldsymbol{S} , \\ H_{zfs} &= H_{zfs}^{ort} + H_{zfs}^{mon} , \\ H_h &= \boldsymbol{I} \cdot \overleftrightarrow{\mathbf{A}} \cdot \boldsymbol{S} , \\ H_{nZ} &= -g_n \beta_n \boldsymbol{B} \cdot \boldsymbol{I} , \\ H_Q &= \boldsymbol{I} \cdot \overleftrightarrow{\mathbf{Q}} \cdot \boldsymbol{I} . \end{aligned} \tag{7}$$

The zfs Hamiltonian in terms of Stevens operators O_k^q (S_x, S_y, S_z) for spin $S = 5/2$ has the following explicit form [25–27]:

$$H_{zfs}^{ort} = B_2^0 O_2^0 + B_2^2 O_2^2 + B_4^0 O_4^0 + B_4^4 O_4^4 . \tag{8}$$

For the case of the C_2-axis parallel to the y-axis as in $BiVO_4$, the monoclinic term takes the form [27]

$$H_{zfs}^{mon} = B_2^1 O_2^1 + B_4^1 O_4^1 + B_4^3 O_4^3 . \tag{9}$$

Some of the B_k^q's are related to D, E, F, and a as [28]

$$\begin{aligned} B_2^0 &= \frac{1}{3} D , \quad B_2^2 = E , \\ B_4^0 &= \frac{1}{180} F + \frac{1}{120} a , \quad B_4^2 = \frac{1}{3} H , \quad B_4^4 = \frac{1}{24} a . \end{aligned} \tag{10}$$

The spin Hamiltonian parameters were determined by a least-squares fit to the experimental data, measured on the crystallographic ab-, bc^*-, and c^*a-plane. Since the hyperfine interaction of Mn^{2+} turns out to be much smaller than the Zeeman and zero field split-

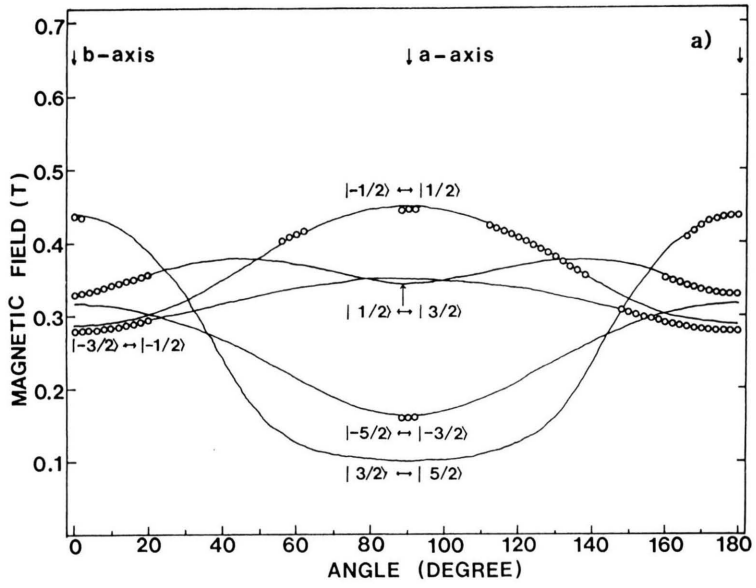

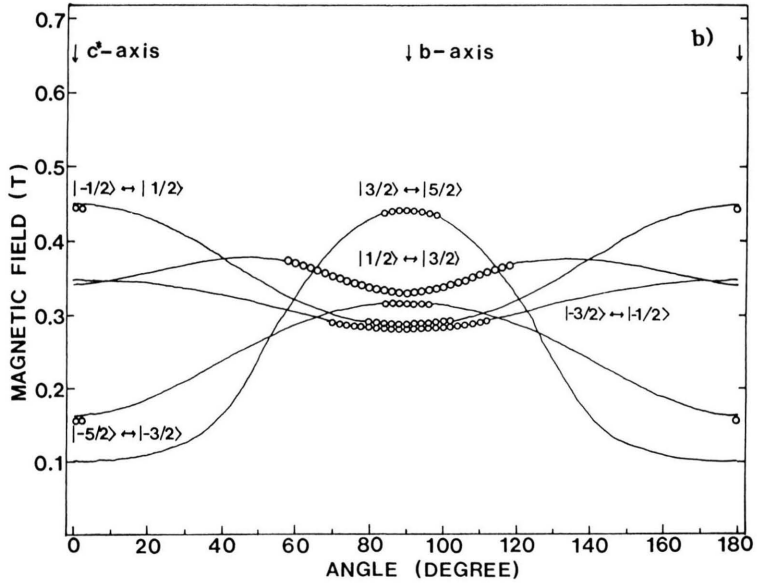

◄ Fig. 9. Rotation patterns of Mn^{2+} in $BiVO_4$, a) in the *ab*-plane, and b) in the *bc**-plane.

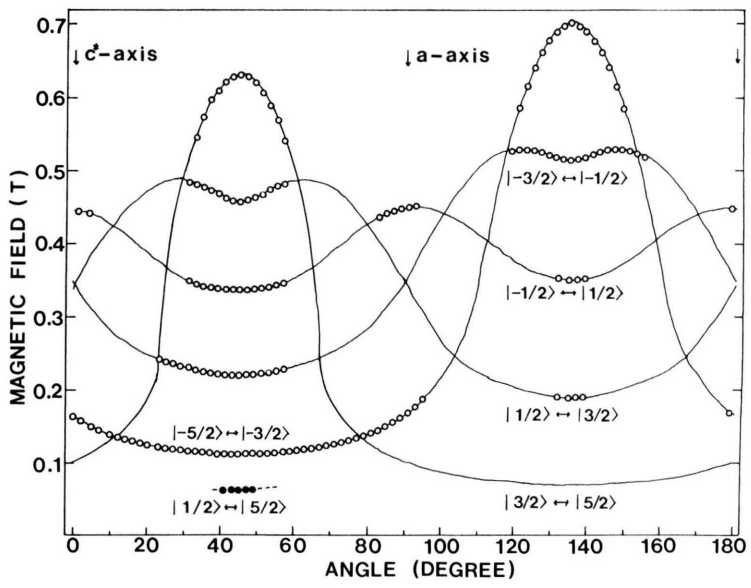

Fig. 10. Rotation pattern of Mn^{2+} in the c^*a-plane of $BiVO_4$.

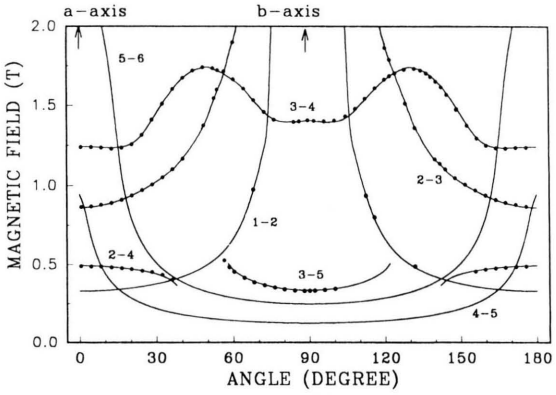

Fig. 11. Rotation pattern of Fe^{3+} in the *ab*-plane of $BiVO_4$, measured at room temperature with the microwave frequency 33.939 GHz (Q-band).

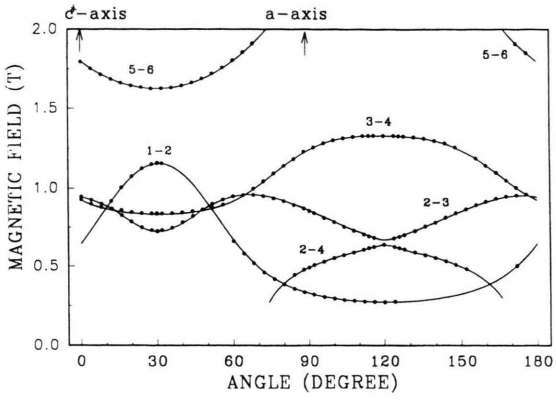

Fig. 12. Rotation pattern of Fe^{3+} in the ac^*-plane of $BiVO_4$, measured at room temperature with the microwave frequency 33.968 GHz.

ting term, first-order perturbation is used for the analysis. The EPR parameters obtained with the orthorhombic approximation [13] for Mn^{2+} in the ferro- and paraelastic $BiVO_4$ are summarized in Table 2 along with those previously reported by Baran et al. [8]. Though the parameters look different from ours [13] and Mn_I of Baran [8], they correspond actually to same center except for the principal axes of **D**-tensor. This point was clarified by us [29]. Experimental data of Mn^{2+} are also analyzed with the monoclinic spin Hamiltonian, and the aspect of low symmetry is discussed in detail in [30].

Though Fe^{3+} is isoelectronic with Mn^{2+}, the only isotope having non-zero nuclear spin is ^{57}Fe ($I = 1/2$) with 2.19% natural abundance. Thus, nearly 98% of the Fe^{3+} ions have no nuclear spin, consequently H_h,

Table 2. EPR parameters of Mn^{2+} ion in the ferro- and paraelastic phase of $BiVO_4$. All units are in GHz except for the g-value.

g	B_2^0	B_2^2	B_4^0	B_4^2	B_4^4	B_2^{-2}	B_4^{-2}	B_4^{-4}	Principal axes	A	Temperature (K)
1.994	0.814	0.4912	0.0005	0.0	0.0				$X = b$ $Y = c^* + 45°$ $Z = a + 45°$	$A_x = 0.27$ $A_y = 0.25$ $A_z = 0.33$	300
1.994	0.000	0.000	0.00							0.25	535
1.994[a]	0.164	0.04	0.0001	0.003	0.0005	1.46	0.0003	0.0001	$X = a$ $Y = -c$ $Z = b$	0.279	300
1.994[a]	0		0.0003		0.00005						650

[a] The units and notation of the Mn_I center (Baran et al. [8]) have been converted for comparison with our data.

Table 3(A). EPR parameters of Fe^{3+} in $BiVO_4$ single crystal at room temperature.

g-tensor	ZFS parameters (10^{-4} cm^{-1})	
$g_{xx} = 1.976$ (1)	$B_2^0 = 467.3$ (7)	$B_2^1 = 1693$ (6)
$g_{xz} = 0.0033$ (26)	$B_2^2 = 2339$ (3)	$B_4^0 = 0.12$ (9)
$g_{yy} = 1.995$ (2)	$B_4^1 = -2.3$ (6)	$B_4^2 = -0.8$ (3)
$g_{zz} = 1.994$ (3)	$B_4^3 = 4$ (1)	$B_4^4 = -0.3$ (3)

(B). The tensors **g** and **D** in the principal axis system.

g-tensor			**D**-tensor		
Components	θ	ϕ (degrees)	Components (MHz)	θ	ϕ (degrees)
$g_{XX} = 1.976$ (1)	100 (7)	0	$D_{XX} = -1306$ (3)	30.5 (1)	0
$g_{YY} = 1.995$ (3)	10 (7)	0	$D_{YY} = -7107$ (8)	120.5 (1)	0
$g_{ZZ} = 1.995$ (2)	90	270	$D_{ZZ} = 8413$ (8)	90	90

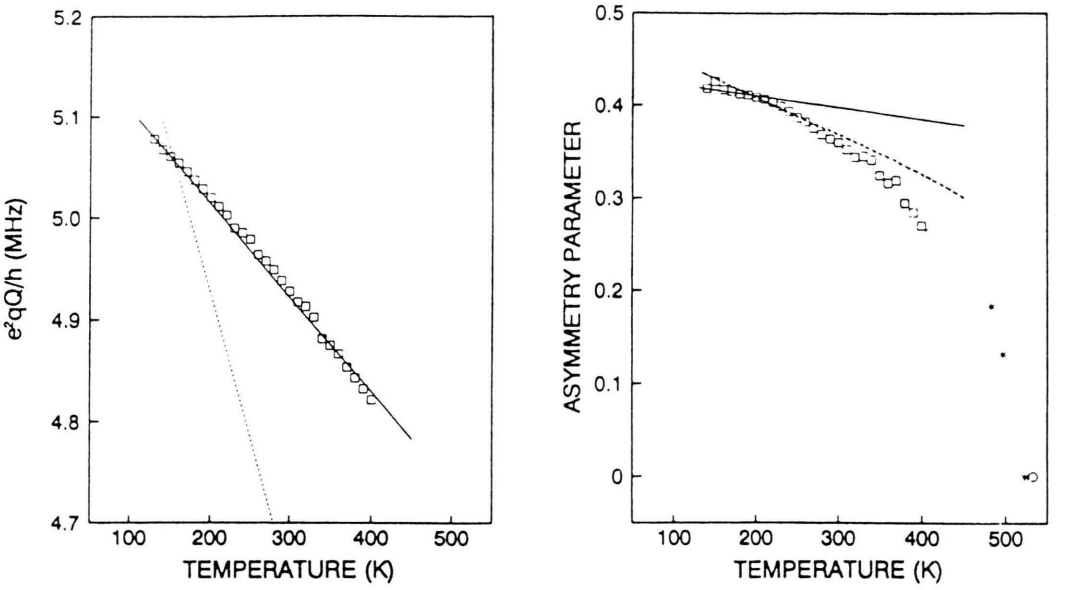

Fig. 13. Temperature dependence of quadrupole parameters of ^{51}V in $BiVO_4$. Data with * in the asymmetry parameter are from [31].

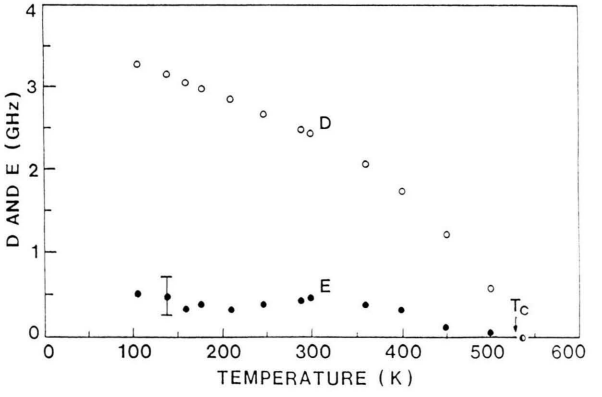

Fig. 14. Temperature dependence of D and E for Mn^{2+} in $BiVO_4$.

H_{nZ}, and H_Q terms are absent for the analysis. The spin Hamiltonian parameters determined by a least-squares fit to the Q-band data are summarized in Table 3 [18].

2.7 Temperature Dependence

The temperature dependence of the quadrupole coupling constant, e^2qQ/h, and asymmetry parameter, η, of ^{51}V has also been investigated, in the temperature range of 130–400 K [16], and the results are shown in Figure 13. Both parameters are found to decrease with increasing temperature. Furthermore, η turns out to decrease continuously down to zero at T_c. This indicates that η can be considered as order parameter of the second-order phase transition of $BiVO_4$.

The temperature dependence of the second order zero field splitting parameters D and E of Mn^{2+} has been also studied, as shown in Figure 14 [14]. Both parameters decrease with increasing temperature. They go to zero almost continuously as the temperature approaches T_c. This dependence is also consistent with the second-order phase transition at T_c.

3. Calculation of Zero Field Splitting Parameters

The zfs parameters for Mn^{2+}, assumed either at the Bi^{3+} or V^{5+} site in $BiVO_4$ crystal, were calculated using the point-charge model and the superposition model [17]. The results are summarized in Table 4. The calculated values of the second-order axial (D) and rhombic (E) component at the Bi^{3+} site turn out to be very similar to the values obtained from our experiment.

Similar calculations for Fe^{3+} were also performed with the superposition model. The results are dis-

Table 4. Zero field splitting parameters calculated by the point charge and superposition model for Mn^{2+} in $BiVO_4$ (in unit of cm^{-1}).

ZFSP	Theoretical model	Bi-site (cal.)	V-site (cal.)	Experimental values
D	pcm	0.0626	0.5517	0.0818
	spm	0.0348	0.9192	
E	pcm	0.0229	0.0984	0.0164
	spm	0.0075	0.1836	

played in Figs. 15 and 16 for D and E, respectively, where $\bar{A}_2$ and $\bar{A}_4$ are intrinsic parameters [18]. These results suggest that the V^{5+} site is a better candidate for substitution of Fe^{3+} in $BiVO_4$. It is worth noticing that, while Mn^{2+} favours the Bi^{3+} site, Fe^{3+} favours the V^{5+} site. This point is discussed further in the following section.

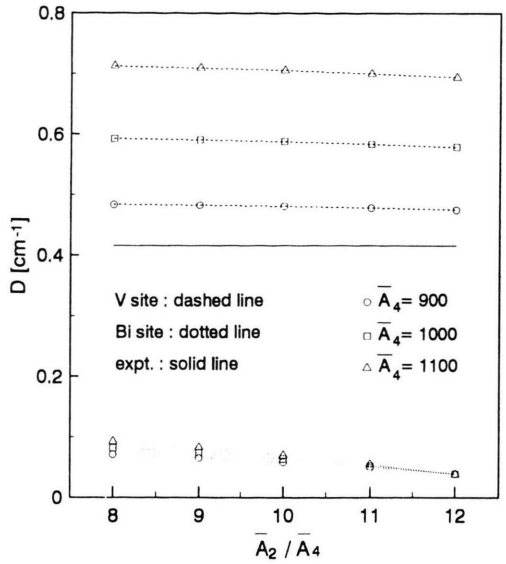

Fig. 15. Calculated D-values of Fe^{3+} in $BiVO_4$ in terms of the superposition model in dependence on the ratio of intrinsic parameters.

4. Discussion

The principal axes systems of the efg tensors of ^{51}V and ^{209}Bi are simply related; the Z-axis is the same along the b-axis, and the X- and Y-axes for ^{209}Bi are rotated by 25° along the b-axis, as shown in Figure 7. The fact that principal axes for ^{51}V coincide with the crystallographic axes of $BiVO_4$ crystal suggests that VO_4^{3-} does not contribute effectively to the efg of $^{51}V^{5+}$. Actually, the perfect tetrahedral bonds give $V_{XX} = V_{YY} = V_{ZZ} = 0$.

The principal X-, Y- and Z-axes of the **D**-tensor for Mn^{2+} in the ferroelastic phase of $BiVO_4$ single crystal are found to lie along the crystallographic b, $c^* + 45°$ and $a + 45°$ axes, respectively. This designation is different from that of Mn_I reported by Baran et al. [8]. Their improper designation of the principal axes is reflected by the largest value of B_2^{-2} compared with $B_2^0(D/3)$ and $B_2^2(E)$ in Table 2. If the axes system of the Mn_I center is transformed to ours, the Mn_I center could be better represented by the parameters of our work [13].

As can be seen in Table 2, the zfs parameters of the Mn^{2+} center in $BiVO_4$ are zero in the paraelastic phase. Since D and E are zero above T_c, the phase transition temperature in $BiVO_4$ can be accurately determined by EPR technique.

Several possibilities of the substitutional site of Mn^{2+} were examined in $BiVO_4$ crystal. First, suppose Mn^{2+} resides at a structural vacancy of the crystal,

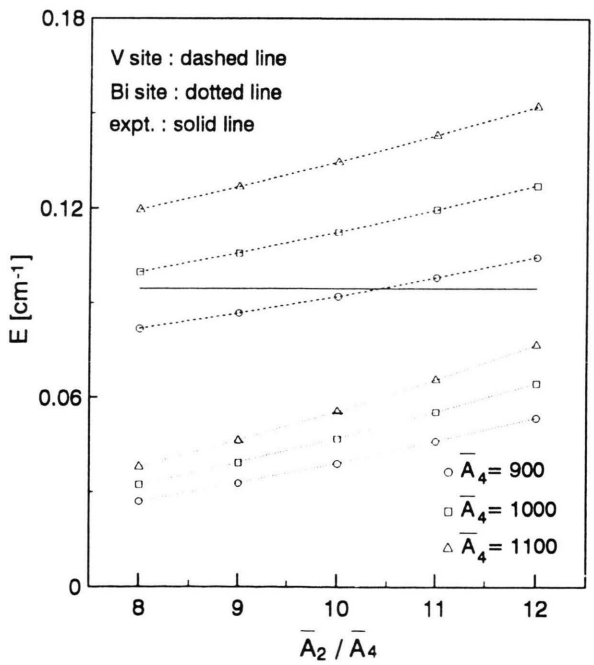

Fig. 16. Calculated E-values of Fe^{3+} in $BiVO_4$, otherwise similar to Figure 15.

then the principal axis of the **D**-tensor in the c^*a-plane should be parallel to the a- or c^*-axis. However, since the experimental results deviate from the a- and c^*-axis, the first possibilities is ruled out. Next, one may propose that Mn^{2+} can occupy either the Bi^{3+} or V^{5+} site. Substitution for Bi^{3+} in $BiVO_4$ seems more reasonable because the principal axes of the **D**-tensor of the Mn^{2+} center are closely associated with the crystallographic axes. As shown in Fig. 17, the Z-axis of the **D**-tensor is along the direction of the shorter Bi-VO_4 bond (7.2514 Å), and the Y-axis is along the longer one (7.3000 Å). This slight difference is well demonstrated in Figure 10. As far as the ionic charge state is concerned, Mn^{2+} is closer to Bi^{3+} than to V^{5+}. The zfs parameters D and E for the Mn^{2+} center in a $BiVO_4$ crystal are calculated using the point charge model (pcm) and the superposition model (spm) [17]. The calculated second-order axial and rhombic zfs parameters at the Bi site turn out to be similar to those from experiment. The spm and pcm give similar results, as summarized in Table 4. Considering all these possibilities, we propose that Mn^{2+} replaces Bi^{3+} without nearby charge compensation. This proposal is consistent with that made by Baran et al. [8].

The substitutional site of Fe^{3+} in $BiVO_4$ is also discussed in terms of experiments and theoretical calculation [18]. One may consider the two possibilities that the Fe^{3+} occupies either the Bi^{3+} or V^{5+} site. The axial zfs value of Fe^{3+} is about five times larger than that of Mn^{2+} which substitutes for Bi^{3+} in $BiVO_4$. The principal axes of the **D** tensor for Fe^{3+} are also quite different from those of Mn^{2+} (Figure 18). In addition, the V-O bonds in the VO_4 tetrahedra make angles of approximately 28° and 120° to the a-axis [19]. These angles are very similar to 30° and 120° of the principal axes for the **D**-tensor with respect to the crystallographic axes system. The larger D value of Fe^{3+} than that of Mn^{2+}, which substitutes for Bi^{3+}, may indicate that Fe^{3+} resides at the V^{5+} site, because the V-O bond length ($\sim$ 1.7 Å) is shorter than the Bi-O bond length ($\sim$ 2.5 Å). Calculation of D and E values of Fe^{3+} in $BiVO_4$ in terms of the point charge and superposition model also favours the V^{5+} site, as displayed in Figures 15 and 16. These facts strongly support that Fe^{3+} substitutes for V^{5+}.

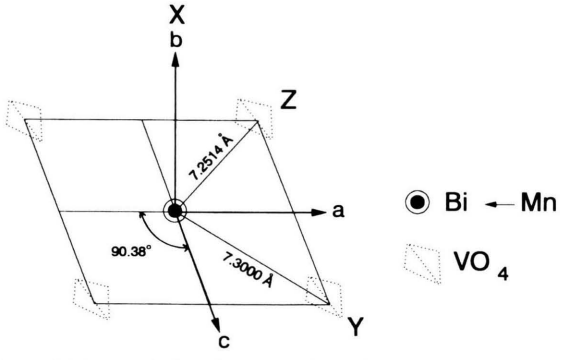

Fig. 17. The relation between the principal axes of the second-order zfs tensor of Mn^{2+} and the crystallographic axes, supporting the proposal of Mn^{2+} substituting for the Bi^{3+} site.

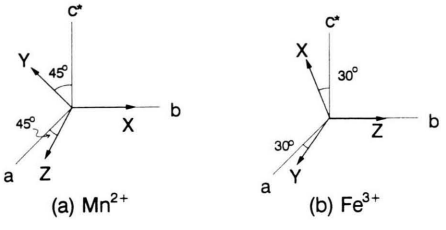

Fig. 18. The principal axes of the second-order zfs tensor of Mn^{2+} and Fe^{3+} in $BiVO_4$ at room temperature.

5. Summary

Nuclear magnetic resonance spectra of ^{51}V and ^{209}Bi in $BiVO_4$ single crystals have been investigated by employing a Varian and a Bruker MSL 200 NMR spectrometers. The quadrupole coupling parameters (e^2qQ/h and η) and the principal axes of the efg tensor for ^{51}V and ^{209}Bi were determined for the first time. From the temperature dependence of the ^{51}V spectrum, it was found that the asymmetry parameter decreases down to zero continuously with increasing temperature to the Curie temperature ($T_c = 523$ K).

Electron paramagnetic resonance of Mn^{2+} and Fe^{3+} ions in $BiVO_4$ have been studied with X- and Q-band EPR spectrometers (Bruker ESP 300). The zfs parameters and the principal axes of **D**-tensor for Mn^{2+} and Fe^{3+} ions have also been determined for the first time. The axial zfs parameter D and the rhombic parameter E were found to decrease with increasing temperature, and they went to zero almost continuously at T_c. These temperature dependences of ^{51}V NMR and Mn^{2+} EPR confirm that $BiVO_4$ crystal undergoes a second order phase transition at 523 K.

The substitutional sites of Mn^{2+} and Fe^{3+} ions in $BiVO_4$ crystals were studied experimentally and theo-

retically. The point charge model and superposition model calculation of zfs parameters support that Mn^{2+} and Fe^{3+} substitute Bi^{3+} and V^{5+}, respectively, in $BiVO_4$ crystal.

Acknowledgements

This work was supported by the Korea Science and Engineering Foundation through the RCDAMP at Pusan National University (1994–1997). I am grateful to Professor P. J. Bray of Brown University, the Chairman of the 13th International Symposium on Nuclear Quadrupole Interactions, for the invitation to give this talk at the Symposium. Thanks are due to Dr. T. H. Yeom and Mr. I. G. Kim for their assistance in preparing the manuscript.

[1] R. S. Roth and J. L. Waring, Amer. Miner. **48,** 1348 (1963).
[2] J. D. Bierlein and A. W. Sleight, Solid State Commun. **16,** 69 (1975).
[3] W. I. F. David, A. M. Glazer, and A. W. Hewat, Phase Trans. **1,** 155 (1979).
[4] A. W. Sleight, H. Y. Chen, A. Ferretti, and D. E. Cox, Mater. Res. Bull. **14,** 1571 (1979).
[5] A. Pinczuk, G. Burns, and F. H. Dacol, Solid State Commun. **29,** 515 (1979).
[6] M. S. Jang, H. L. Park, J. N. Kim, J. H. Ro, and Y. H. Park, Japan J. Appl. Phys. **24-2,** 506 (1985).
[7] A. F. Volkov, L. A. Ivanova, and Y. N. Venevtsev, Sov. Phys. Solid State **14,** 617 (1978).
[8] N. P. Baran, V. I. Barchuk, V. G. Grachev, and B. K. Krulikovskii, Sov. Phys. Crystallogr. **30,** 410 (1985).
[9] N. P. Baran, V. I. Barchuk, V. G. Grachev, and B. K. Krulikovskii, Sov. Phys. Solid State **28,** 485 (1986).
[10] S. V. Akimov, E. L. Mnushkina, and E. F. Dudnik, Sov. Phys. Tech. Phys. **27,** 500 (1982).
[11] S. H. Choh, E. Y. Moon, Y. H. Park, and M. S. Jang, Japan J. Appl. Phys. **24-2,** 640 (1985).
[12] A. R. Lim, S. H. Choh, and M. S. Jang, J. Phys.: Condens. Matter **4,** 1607 (1992).
[13] T. H. Yeom, S. H. Choh, and M. S. Jang, J. Phys.: Condens. Matter **4,** 587 (1992).
[14] T. H. Yeom, C. Rudowicz, and S. H. Choh, Ferroelectrics **156,** 249 (1994).
[15] T. H. Yeom and S. H. Choh, 27th Congress Ampere, Abstract P533 (Kazan 1994).
[16] T. H. Yeom, A. R. Lim, S. H. Choh, and K. S. Hong, J. Korean Phys. Soc. **26,** 670 (1993).
[17] T. H. Yeom, S. H. Choh, and M. L. Du, J. Phys.: Condens. Matter **5,** 2017 (1993).
[18] T. H. Yeom, S. H. Choh, M. L. Du, and M. S. Jang, Phys. Rev. B **53,** 3415 (1996).
[19] W. I. F. David and I. G. Wood, J. Phys. C **16,** 5127 (1983).
[20] I. G. Wood and A. M. Glazer, J. Appl. Crystallogr. **13,** 217 (1980).
[21] L. P. Avakyants, A. M. Antonenko, E. F. Dudnik, D. F. Kiselev, I. E. Mnushkina, and M. M. Firsova, Sov. Phys. Solid State **24,** 1411 (1982).
[22] A. R. Lim, S. H. Choh, and M. S. Jang, Ferroelectrics **94,** 389 (1989).
[23] P. P. Man, S. H. Choh, and J. Fraissard, Solid St. Nucl. Mag. Res. **3,** 231 (1994).
[24] CRC Handbook for Chemistry and Physics, 58th Ed. (CRC Press, 1977) E-69 and E-71.
[25] J. R. Pilbrow, Transition Ion Electron Paramagnetic Resonance, Clarendon Press, Oxford 1990, Chapt. 6.
[26] S. K. Misra and C. Rudowicz, Phys. Status Solidi (b) **147,** 677 (1988).
[27] C. Rudowicz, Mag. Res. Rev. **13,** 1 (1987).
[28] D. G. McGavin, J. Mag. Res. **74,** 19 (1987).
[29] T. H. Yeom, S. H. Choh, and C. Rudowicz, Acta Physica Polonica A **82,** 503 (1992).
[30] T. H. Yeom, C. Rudowicz, S. H. Choh, and D. G. McGavin, Phys. Rev. (submitted).
[31] S. Segel, Solid State Commun. **54,** 403 (1985).